Biogeosciences Discuss., 11, 7853–7900, 2014
www.biogeosciences-discuss.net/11/7853/2014/
doi:10.5194/bgd-11-7853-2014

Biogeosciences Discussions
Open Access

A model of the methane cycle, permafrost, and hydrology of the Siberian continental margin

D. Archer

University of Chicago, Chicago, USA

Received: 15 April 2014 – Accepted: 7 May 2014 – Published: 3 June 2014

Correspondence to: D. Archer (d-archer@uchicago.edu)

Published by Copernicus Publications on behalf of the European Geosciences Union.

Abstract

A two-dimensional model of a passive continental margin was adapted to the simulation of the methane cycle on Siberian continental shelf and slope, attempting to account for the impacts of glacial/interglacial cycles in sea level, alternately exposing the continental shelf to freezing conditions with deep permafrost formation during glacial times, and immersion in the ocean in interglacial times. The model is used to gauge the impact of the glacial cycles, and potential anthropogenic warming in the deep future, on the atmospheric methane emission flux, and the sensitivities of that flux to processes such as permafrost formation and terrestrial organic carbon (Yedoma) deposition.

Hydrological forcing drives a freshening and ventilation of pore waters in areas exposed to the atmosphere, which is not quickly reversed by invasion of seawater upon submergence, since there is no analogous saltwater pump. This hydrological pump changes the salinity enough to affect the stability of permafrost and methane hydrates on the shelf.

Permafrost formation inhibits bubble transport through the sediment column, by construction in the model. The impact of permafrost on the methane budget is to replace the bubble flux by offshore groundwater flow containing dissolved methane, rather than accumulating methane for catastrophic release when the permafrost seal fails during warming. By far the largest impact of the glacial/interglacial cycles on the atmospheric methane flux is attenuation by dissolution of bubbles in the ocean when sea level is high. Methane emissions are highest during the regression (soil freezing) part of the cycle, rather than during transgression (thawing).

The model-predicted methane flux to the atmosphere in response to a warming climate is small, relative to the global methane production rate, because of the ongoing flooding of the continental shelf. A slight increase due to warming could be completely counteracted by sea level rise on geologic time scales, decreasing the efficiency of bubble transit through the water column. The methane cycle on the shelf responds to climate change on a long time constant of thousands of years, because hydrate is

excluded thermodynamically from the permafrost zone by water limitation, leaving the hydrate stability zone at least 300 m below the sediment surface.

1 Introduction

1.1 The Siberian continental shelf system

The Siberian Arctic continental shelf has been the focus of attention from scientists and the public at large for its potential to release methane, a greenhouse gas, in response to climate warming, a potential amplifying positive feedback to climate change (Shakhova, 2010; Westbrook, 2009). The goal of this paper is to simulate the geophysical and carbon cycle dynamics of the Siberian continental margin within the context of a basin- and geologic time-scale mechanistic model of the coastal margin carbon cycle called SpongeBOB (Archer et al., 2012). An initial configuration of sediment structure and composition was spun up over 62 million simulated years. Then the model is driven by cyclic changes in sea level and air temperature resulting from glacial cycles, to simulate the impact of the hydrological pressure head and permafrost formation on the fluid flow and methane cycle on the shelf. Finally, an 100 000 year interglacial interval in the simulation is subjected to anthropogenic warming of the overlying water and potential 60 m changes sea level.

1.1.1 Permafrost

One component of the problem is a wedge of frozen sediment (permafrost) submerged beneath the ocean on the continental shelf of Siberia, left behind from glacial time when the shelves were exposed to the frigid atmosphere by lowered sea level (Romanovskii and Hubberten, 2001). The ice is thought to provide a seal to upward migration of methane gas (Shakhova et al., 2009), especially where ancient fresh groundwater flow produced a layer of very high saturation ice infill, a formation called the Ice Complex in

Siberia (Romanovskii et al., 2000), although there are high ice saturations found in the Alaskan Arctic as well (Zimov et al., 2006).

With inundation by the natural sea level rise over the last 10+ thousand years, the permafrost is transiently melting, although the time constant for this is generally long enough that significant frozen volume remains, especially in shallower waters which were flooded more recently (Khvorostyanov et al., 2008a; Nicolsky and Shakhova, 2010; Romanovskii and Hubberten, 2001; Romanovskii et al., 2004; Shakhova et al., 2009; Taylor et al., 1996). Even overlying water at the freezing temperature can provoke subsurface melting by providing a warmer boundary condition against which geothermal heat establishes the subsurface temperature profile, but with climate warming, the waters could surpass the freezing temperature, allowing heat to flow from above as well as below (Khvorostyanov et al., 2008b).

Elevated methane concentrations have been measured in the water column over the Siberian shelf, even in areas of shallow water where the permafrost should still be strongly intact (Shakhova, 2010; Shakhova et al., 2005). Chemical and isotopic signatures of hydrocarbons adsorbed onto surface sediments indicate a thermal origin (Cramer and Franke, 2005), suggesting that the methane is produced many kilometers deep in the sediment column. The apparent ability for this methane to transverse the barrier of the Ice Complex has been attributed to hypothesized openings in the ice (called “taliks”), resulting from lakes or rivers on the exposed shelf, or geologic faults (Nicolsky and Shakhova, 2010; Romanovskii et al., 2004; Shakhova et al., 2009).

1.1.2 Salt

Dissolved salt in the pore waters can have a strong impact on the timing of thawing permafrost (Nicolsky and Shakhova, 2010; Shakhova et al., 2009). The salinity of the pore waters of a sediment column exposed to the atmosphere can be flushed out by hydrological groundwater flow, driven by the pressure head from the elevated terrestrial water table above sea level. Ground waters tend to be fresh, a product of the hydrological cycle, rather than saline as in marine sediments. The boundary between fresh

and salty pore water tends to intersect the beach at the water's edge (Moore et al., 2011). From there, the boundary tends to dip landward, to a depth of approximately 40 m below sea level for every 1 m of elevation of the table water. The ratio of water table elevation to freshwater lens depth is driven by the relative densities of fresh and salt water, as the fluid seeks an isostatic balance in which the fresh water displaces an equal mass of salt water (Verrjuit, 1968).

The SpongeBOB model has been modified to simulate the processes responsible for these observations. We do not attempt to simulate a detailed outcropping history over the 62 million year spinup time of the sediment column, but rather demonstrate the general process by subjecting the nearly complete sediment column to a one-time sea level lowering, exposing the continental shelf to groundwater forcing. After a few million years, the sediment column subsides, due to compaction and absence of sediment deposition, resulting in a sediment column that has been considerably freshened by the atmospheric exposure. The model indicates that this freshening persists for millions of years, because there is no corresponding "salt-water pump" during high sea-level stands. This behavior is consistent with the discovery of vast nearly fresh aquifers in currently submerged continental shelf regions around the world (Post et al., 2013), left over from groundwater forcing during glacial time.

1.1.3 Carbon

The other component of the Arctic methane story is the Yedoma, deposits of wind-blown dust and organic carbon that accumulated on the coastal plains of exposed continental shelves during glacial times (Zimov et al., 2006). These deposits contain a substantial fraction of organic carbon, consisting of grass roots and remains, preserved by the freezing conditions. When they thaw, they begin to release CO_2 and methane to the atmosphere (Dutta et al., 2006; Schuur et al., 2008; Zimov et al., 2006). Oxidation of the carbon can give off enough heat to accelerate the melting driven by primary climate forcing (Khvorostyanov et al., 2008b).

2 Model description

2.1 Previously published model formulation

SpongeBOB is a two-dimensional basin spatial-scale and geological time-scale model for the methane cycle in continental margin sediments. The model, configured for a passive margin basin, was described by Archer et al. (2012), as applied to the Atlantic coast of the United States. The model attempts to "grow" a sediment column based on first principles or parameterizations of sediment and pore water physical and chemical dynamics. The approach integrates our understanding of the carbon and methane cycles within the evolving sediment column matrix, providing constraints to the rates and processes that may inform the response of the system to future changes in climate. The prognostic model can also be applied in sensitivity studies to assess the impact of large-scale geophysical drivers such as ocean temperature and carbon cycle dynamics that might have shaped the evolution of the sedimentary methane cycle in the geologic past.

Sediment is delivered from the coast of the model as riverine material, and it settles according to a parameterization based on grain size, with finer material advecting further offshore before deposition. The organic carbon concentration of the depositing material is determined in the model as a function of water depth at the time of sedimentation. Rather than attempt to simulate the complex biogeochemical dynamics of the ocean and surficial sediments (early diagenesis), the POC fraction, and the H/C ratio of the organic matter, are specified by a parameterization based on water-depth to reproduce the observed patterns of sediment surface POC deposition, as a driver to the subsurface model.

The H/C ratio of the depositing organic matter limits the potential extent of methane production from the organic matter. The degradation rate of organic carbon is estimated based on its age, a relationship that captures many orders of magnitude of variability in the natural world (Middelburg et al., 1997). The reaction pathways presume a reactive intermediate H_2, which either reduces SO_4^{2-} if it is available or it reacts with DIC to

produce methane. Isotopic fractionation of CO_2, CH_4, and radioiodine are simulated by maintaining parallel concentration fields of different isotopologs, and applying fractionation factors to the chemical kinetic rate constants or equilibrium conditions. Dissolved methane in the pore water has the potential to freeze into methane hydrate or degas into bubbles, depending on the T, P, and CH_4 concentrations.

Sediment compaction drives pore fluid advection through the sediment column, but the fluid flow is also focused in some simulations by ad hoc vertical channels of enhanced permeability, to simulate in at least a qualitative way the impact of heterogeneity in the fluid flow on the characteristics of the tracer field. Methane hydrate is concentrated in these channels by focused upward flow, and the pore-water tracers in the channels resembles that of hydrate-bearing regions (in SO_4^{2-} concentration and 129-Iodine ages).

Most of the model configuration and formulation was described by Archer et al. (2012). Here we describe in detail the new modifications required to simulate groundwater hydrological flow and permafrost formation.

2.2 Groundwater hydrology

2.2.1 Pressure head

When the sediment column is exposed to the atmosphere, the pressure field from the variable elevation of the water table (the pressure head) begins to affect the fluid flow. The pressure head for a fluid particle at the depth of the water table varies as

$$P_{\text{head}}(z) = g \int_{z}^{z_{\text{wt}}} \rho_{\text{seawater}} \mathrm{d}z$$

where z_{wt} is the elevation of the water table. The pressure head at each depth in the domain is a function of the physical water table height above it and the density anomalies integrated from the water table to the depth of the point in question. The

pressure head resulting from a varying water table can therefore be altered at depth by variations in pore fluid density driven by salinity or temperature.

2.2.2 Fluid flow

The pressure head acts in concert with the excess pressure P_{excess} to drive horizontal Darcy flow through the sediment, as

$$u_{\text{Darcy},i\rightarrow i+1} = \frac{k_{h,i} + k_{h,i+1}}{2\mu} \frac{(P_{\text{excess},i} - P_{\text{excess},i+1}) + (P_{\text{head},i} - P_{\text{head},i+1})}{(\Delta x_i + \Delta x_{i+1})/2}$$

while the vertical flow in the model is driven only by compaction pressure

$$w_{\text{Darcy},j\rightarrow j+1} = \frac{k_{v,j}}{\mu} \frac{P_{\text{excess},j} - P_{\text{excess},j+1}}{(\Delta z_j + \Delta z_{j+1})/2}$$

The value of P_{excess} is determined from the porosity and sediment load of the sediment in each grid box, as described in (Archer et al., 2012). An assumed sediment rheology is used to calculate the load-bearing capacity of the solid matrix within a given grid cell. P_{excess} is calculated by assuming that the load of the solid phase overlying the grid cell is carried by the sum of the load-bearing capacity of the sediment (a one-to-one function of porosity), and P_{excess} carried by the fluid phase, which is calculated by difference.

In previous versions of the SpongeBOB model, the fluid flow was calculated explicitly, each time step, as a function of P_{excess} at the beginning of the time step. Numerical stability motivated a modification of the vertical flow to an implicit numerical scheme, which finds by iteration an internally consistent array of vertical flow velocities and resulting P_{excess} values from a time point at the end of the time step. Ocean and atmosphere models often use this methodology for vertical flow. A benefit to this change is stability in the vertical flow field, as a reduction in the numerical noise in the flow, which causes trouble when it interacts dynamically with other aspects of the model such as

ice formation. Implicit schemes can be more efficient computationally, but in this case the execution time is not improved by the implicit method, just the stability.

Note that the flow scheme in its formulation is entirely elastic, whereas in reality, pore fluid excluded by the pressure of a sediment column above sea level, for example, where it is uncompensated by buoyancy in seawater, should remain excluded when sea level rises again, like toothpaste from the tube. However, my attempts to embed this plastic behavior into an implicit solver failed to converge.

2.2.3 Water table depth

The model maintains z_{wt}, the elevation of the water table within the sediment column, as a continuous variable that ranges through the discreet vertical grid of the model. The formulation allows boxes to be empty of water or partially "saturated" at the top of the fluid column. It was necessary to treat z_{wt} as a continuous variable because of the impact of the pressure head on the fluid flow.

The evolution of the height of z_{wt} is determined by changes in the relative volumes of fluid and air phases. In grid cells at and above the depth of the water table, the air volume is computed such that the porosity of the cell relaxes toward the drained condition, in which $P_{excess} = 0$. In this way the outcropping grid cell provides an upper pressure boundary condition for the model, as opposed to grid columns which are entirely submerged, which take the sea floor as a $P_{excess} = 0$ boundary condition.

In outcropping grid cells, any decrease in fluid volume in the course of a time step is offset by a corresponding increase in the air volume. Any air volume in a time step, in turn, is vulnerable to replacement by precipitation from the atmosphere (recharge). A maximum possible groundwater recharge rate of 0.1 m per year is imposed, but in these simulations, given the very shallow land surface elevation gradient, the capacity for subsurface flow to accommodate recharge is much lower than this, of order a few millimeters per year. The depth of the water table in these simulations corresponds very closely with the depth of the sediment surface, as any unsaturated soil produced by lateral flow is replenished by recharge.

2.2.4 Canyons

The model as described so far represents a laterally homogeneous slab, a poor approximation for hydrology above sea level because of the formation of canyons and river networks in a real drained plateau. The depth of the water table in a river canyon is depressed, relative to the surroundings, to the depth of the canyon. The water table is higher in between the canyons because of recharge, and the difference in head drives lateral flow, the canyons acting to drain the sediment column.

The model formulation has been altered to represent this mechanics in a simplified way. Rather than expand the model into the full third dimension, the 2-D field of the model is held to represent the sediment column at a hypothetical ridge crest, as altered by an adjacent canyon. The canyon elevation is represented by z_{canyon}, and its width by a scale Δy_{canyon}. A cross-column flow velocity $v_{Darcy,j}$ is calculated as

$$v_{Darcy,j} = \frac{k_{h,j}}{\mu} \frac{(P_{head,\,canyon} - P_{head})}{\Delta y_{canyon}}$$

where $P_{head,\,canyon}$ is the pressure head as a function of depth in the hypothetical canyon, calculated assuming that the water table outcrops at z_{canyon}, and that the temperatures in the sediment column have adjusted to the formation of the canyon, such that the near-surface geothermal gradient is the same between the hypothetical canyon and the bulk sediment column. The lateral "drainage" flow ($v_{Darcy,j}$) drives vertical velocities by continuity.

The horizontal distance scale Δy_{canyon} is somewhat arbitrary and difficult to constrain, given that in the reality of river networks the distance to the nearest canyon from any point in the domain is likely to be a function of altitude, distance from the coast, and time. Another poorly resolved factor is the depth of the canyon. In reality, canyons cut into a plateau following a dynamic that erosion is proportional to slope, but stops at sea level. As a simplification the model is set to hold the canyon depth at current sea level.

The canyon mechanism accelerates the freshening of the sediment column by providing a pathway for the escape of the salt water, although it was found that the net effect in the model is not dramatic (results shown below), in part because the canyon drainage mechanism only acts on pore fluids above sea level, while the hydrological freshwater pumping mechanism reaches much deeper than sea level.

2.3 Permafrost

The numerical treatment of ice formation in the pore space in any given time step is based on the energy constraint that the maximum extent of ice freezing, for example, would release enough latent heat to raise the temperature of the grid cell to the freezing point.

$$\text{Freeze}_{\max} = \frac{\Delta T \cdot c_p \cdot V}{H_{\text{fusion}} \cdot \text{MW}_{\text{ice}}}$$

where ΔT is the temperature difference from equilibrium (which is a function of salinity and pressure), c_p is the heat capacity of the grid cell overall (linear average of the material in the cell), H_{fusion} is the heat of fusion of ice, and MW_{ice} is the molecular weight. The actual extent of freezing imposed in a time step is taken to be 1 % of $\text{Freeze}_{\max}$, to prevent oscillations of the salinity, hence the freezing temperature, of the cell. Although the kinetics of freezing imposed by this formulation are much slower than would be realistic (given a time step of 0.02 years), the model forcing, due to changes in surface temperature, sea level, and subsurface diffusion of heat, is slow enough that the model relaxes nearly to an equilibrium condition, where the elevated salt concentration in the pore water drives a freezing point depression that matches the local temperature. A limiter in the code prevents more than 99 % of the fluid in a grid cell from freezing, but the thermodynamic equilibrium salinity is used to calculate, for example, the stability of methane hydrate, to prevent the numerical limiter from affecting the thermodynamic availability of water to drive chemical reactions.

This model formulation implies that the salinity of pore fluid in subfreezing conditions (the permafrost zone) is independent of the original salinity of the bulk sediment column, but is rather determined only by the freezing-point depression implied by the temperature. If the original column is relatively fresh, there will be a smaller volume of pore fluid at a subfreezing temperature than if it is originally salty (see for example Fig. 4 in Nicolsky and Shakhova, 2010), but the activity of the water (a correlate of the salinity) is set by the temperature and the thermodynamics of pure ice, which are the same in the two cases. Layers of high-salinity unfrozen brines called cryopegs (Gilichinsky et al., 2005; Nicolsky et al., 2012) are consistent with this formulation. The high salinity (low activity of water) in the permafrost zone has the practical impact of excluding methane hydrate from permafrost soils that are significantly colder than freezing (results shown below).

Permafrost formation has several impacts on the methane cycle in the model. Biogenic methanogenesis is assumed stopped in the ice fraction of a grid cell (which approaches unity but never reaches it in the model, due to exclusion of salt into brine). Bubble transport in the model balances bubble production, driven by a small and not very well constrained standing bubble concentration within the pore space. It is generally assumed (Shakhova et al., 2010b) that permafrost inhibits gas transport through the sediment column, both based on sediment column carbon and hydrogen budgets (Hunt, 1995) and on the tight seal provided by the ice complex. The seal provided to Arctic lakes, which can drain overnight if the seal is breached, also lends credence to this idea. In the model, this effect was simulated by stopping gas transport completely when a grid cell exceeds 50 % ice fraction.

2.4 Atmospheric methane fluxes

Bubbles emerging from the sediment column into the water column of the ocean may dissolve in the water column, or they may reach the sea surface, a direct methane flux to the atmosphere (Westbrook et al., 2009). In the model, bubble dissolution in the water column is assumed to attenuate the bubble flux according to the water depth

with an e-folding attenuation scale of 30 m (Gentz et al., 2014; Portnov et al., 2013; Westbrook et al., 2009). In reality, a low-flux gas seep, producing small bubbles, will probably not reach as far into the water column as a 30 m scale height, while a faster seep can reach further. For land grid points (exposed to the atmosphere by lowered sea level), any upward bubble flux is assumed 100 % released to the atmosphere. The model neglects methane oxidation in soils, as well as many other terrestrial processes such as thaw bulbs beneath bodies of water (Walter et al., 2006), and the seasonal cycle of melting and thawing in the surface active layer. In short, the methane fluxes to the atmosphere computed from the model runs are crude, and underlain by a sedimentary methane cycle with large uncertainties, intended to capture the main sensitivities to various processes rather than to provide strong quantitative constraint to the fluxes in the real world.

2.5 Comparison with previous models

The dynamics of the permafrost layer, and its present state, have been extensively modeled to produce detailed maps of the crust and sediment structure (Gavrilov et al., 2003; Nicolsky and Shakhova, 2010; Nicolsky et al., 2012; Romanovskii and Hubberten, 2001; Romanovskii et al., 2005). The crust underlying the continental shelf area has been alternately subsiding and rising in blocks called horsts and grabens (Nicolsky et al., 2012). The sediment cover on the horsts is much thicker than it is in the grabens. SpongeBOB, an idealized two-dimensional model, does not address this complexity, but the thickness of the sediment cover on the shelf ranges from 5–10 km, reminiscent of the horsts (subsiding blocks).

Methane hydrate modeling has been done in the Arctic applied to the Siberian continental slope (Reagan, 2008; Reagan and Moridis, 2009; Reagan et al., 2011), but only one calculation has been done in the context of permafrost formation (Romanovskii et al., 2005), as found on the shelf. Romanovski (2005) modeled the extent of the methane hydrate stability zone through glacial cycles, but apparently based the calculations on marine salinity values when calculating the stability of hydrate, while I argue

that in sub-freezing conditions (in the permafrost zone) the only water available for hydrate formation will be in a saline brine that would be in equilibrium with ice at the local temperature. These high salinities restrict hydrate stability to near the base of the permafrost zone and deeper. In the Mackenzie Delta, hydrate was detected in a core drilled into onshore permafrost soils (Dallimore and Collett, 1995), but only at depths greater than 300 m, near the base of the permafrost where the temperature is close to freezing.

3 Results

3.1 Initial spinup

The model setting was grown for 62 million years of model time. The initial spinup used a relatively coarse resolution as shown in Fig. 1a. For the glacial/interglacial experiments, the initial condition was interpolated to a higher resolution grid in the vertical, as shown in Fig. 1b. Particulate organic carbon (POC) concentrations are highest just off the shelf break (Fig. 2), because this is where most of the sediment is deposited, and because the sedimentary material is richest in POC in shallow ocean water depths in the model (Archer et al., 2012). The unchanging sea level in the spinup period kept the sediment surface from outcropping, resulting in nearly uniform marine salinity throughout the model domain (Fig. 3a). Methane concentration (Fig. 4a) closely mirrors the solubility of dissolved methane, resulting in near saturation concentrations through most of the model domain (Fig. 4b). As in the previous model simulations (Archer et al., 2012), the imposition of permeable channels has a strong effect on the chemistry of the permeable grid cells (Fig. 4d), although the impact on the integrated model behavior, such as the methane flux to the atmosphere, was small, so for clarity model results neglecting these channels will be shown.

3.2 Impact of freshwater hydrology

When sea level drops such that the land surface outcrops to the atmosphere, the pore fluid becomes subject to the pressure head driving it seaward, and to fresh water recharge from precipitation. The pressure head forcing and the buoyancy of the sediment fluid column combine to create a mechanism to excavate salinity from the upper sediment column. Initially after sea level fall, there is a pressure head gradient extending throughout the sediment column, provoking lateral flow at all depths. As the pore fluid at the surface is replaced by fresh runoff, the lighter density of that fluid tends to diminish the pressure head gradient in the deeper sediment column. The deeper pressure gradient and flow approach zero as the fresh water lens in the outcropping region approaches an isostatic equilibrium condition known as the Ghyben–Herzberg relation (Moore et al., 2011), in which each meter elevation of the water table is compensated for by about 40 m of fresh water below sea level, determined by the difference in densities of fresh and salt water.

In an attempt to create this condition within the model, two simulations are presented in which sea level was decreased by 30 and 120 m, respectively, and held there for millions of years (Fig. 5). The 30 m drop experiment produced land outcrop in about 1/4 of the model domain, with the predicted equilibrium Ghyben–Herzberg halocline reaching about 1200 m maximum depth. The model salinity relaxes into close agreement with the predicted halocline, lending support to the model formulation for density, pressure head, and fluid flow. As time progresses further, the outcropping land surface subsides (there is no land deposition at this time in the simulation, and a loss of buoyancy when the sediment is out of water), until it drops below the new lowered sea level value after about 2.5 Myr. The sequence of events leaves behind a persistent fresh water lens below sea level.

Variants of this experiment were done with differing values of the lateral distance to drainage canyons in the model, which provide a pathway for fluid loss in sediments above sea level. When a hypothetical canyon is located 10 km from the SpongeBOB

slab, the model salinity approaches equilibrium on a time scale of about 300 kyr (Fig. 6). When the canyon is 100 km distant or nonexistent, the equilibration time scale is about 500 kyr. The rest of the simulations in this paper were done using the relatively low-impact 100 km canyon spacing.

When sea level is lowered by 120 m, the sequence of events is similar, except that the pressure head is so high that to satisfy the Ghyben–Herzberg relation would require fresh pore waters at many kilometers depth, even deeper than bedrock on the "continental" side of the model domain. Because of the low permeability of the deepest sediment column, the freshwater pumping groundwater mechanism is unable to reach these deepest pore waters, which therefore remain salty. The time scale for establishing a significant freshening of the upper kilometer of the sediment column is still on the order of 100–500 kyr, and the subsequent subsidence time of the sediment column in the model, until it drops below the new lowered sea level, takes about 10 Myr. In both cases, subsidence of the exposed sediment column prevents the sediment surface in the model from remaining above sea level indefinitely.

The salient observation from both of these simulations is the persistence of the fresh pore water lens after its resubmergence in the salty ocean. Groundwater flow, driven by the pressure head, provides a means of pumping fresh water into the sediment column that has no counterpart for salty ocean water. Submerged pore waters near the sediment surface tend to pick up salt by diffusion in the model, but this is much slower than the ground water pumping mechanism, and its depth reach is much shallower. Any exposure of the continental shelf to the atmosphere will tend to ratchet down the salinity of the pore waters on the shelf, consistent with the recent discovery of vast freshwater aquifers on global continental shelves (Post et al., 2013), and in particular the lower-than-marine salinities of the pore waters measured in submerged surface Arctic sediments (summarized by Nicolsky et al., 2012). The impact of the groundwater pump on the methane cycle in the upper sediment column is profound and long-lasting in the model (Fig. 7).

The final, resubmerged state of the 120 m drop experiment is taken as the initial condition for glacial/interglacial cycle forcing, described in the next section, through which the behavior of this "prefreshened" initial condition is compared with that from a "pure marine" (still salty throughout) initial condition (Fig. 3b).

3.3 Glacial cycles

3.3.1 Setup and forcing

Beginning from an entirely submerged initial condition, the model is subjected to 100 kyr sawtooth cycles of sea level ranging between −120 to +20 m from the initial sea level (starting at −120 for prefreshened, 0 for pure marine) (Fig. 8a). We show a suite of model simulations intended to isolate the impacts of various component processes.

The simplest scenario (SL) varies the sea level while keeping the air and water temperatures time-invariant. The sea-level air temperature is maintained at 0 °C. This simulation is nearly permafrost-free, with a small exception where the altitude of the sediment surface is much higher than sea level (due to the decrease in temperature with altitude in the atmosphere). There is no deposition of sediment above sea level in this simulation. Permafrost formation is added in simulation GL, in which the air temperature ramps down to −16 °C at sea level, linearly with the glacial sea level fall (Fig. 8b). Deposition of organic-rich sediments when the surface is exposed to the atmosphere (Yedoma: represented as accumulation of 10 m in 100 kyr, with 30 % POC) is added in scenarios SL + LD and GL + LD (LD for land deposition). The atmospheric temperature impact of a global warming scenario (GW) is also shown in Fig. 8b, beginning at 400 kyr, and compared with an extended-interglacial control forcing (Ctl). The potential impact of geologic-time scale sea level rise is added to the global warming scenario in simulation GL + SL.

3.3.2 Salinity and ice

In the "prefreshened" initial condition (Fr), millions of years have elapsed since the previous exposure of the sediment to hydrological forcing, but a core of fresh water remains. Salinities near the sediment surface have grown saltier due to diffusive contact with the salty ocean (Fig. 9, left). A fully marine initial condition (Mar) (Fig. 9, right) was initialized from the unfreshened case, in which sea level was held at a fixed value throughout the 65 Myr spinup of the sediment column. The salinities are nearly uniform in this case.

When the sediment surface is re-exposed to the atmosphere during an interval of low sea level, in the absence of ice formation, the surface layer tends to freshen relatively quickly due to the hydrological forcing, but a subsurface salinity maximum persists (Fig. 9c and d). However, if the air temperatures are cold enough to form ice, surface salinities in the model increase to up to nearly 190 psu, in both prefreshened and pure marine cases (Fig. 9e and f). By the next interglacial time (Fig. 9g and h), ice near the sediment surface has melted enough for near-surface pore waters to reach relatively low salinities.

3.3.3 Pressure and flow

The effect of the sea level and permafrost forcing on the pressures and flow velocities are shown in Fig. 10. On a spatial scale of the entire model domain (Fig. 10, left), the highest driving pressures are found at the base of the sediment column, underneath the region of maximum sediment accumulation (the depocenter just off the shelf break). Changes in sea level drive large fluctuations in the pressure head (contours) extending to bedrock. In the near-surface continental shelf (Fig. 10, right), the driving pressure variations are dominated by the pressure head driven by sea level changes. The formation of permafrost (Fig. 10e and f) seals the upper sediment column to fluid flow. When sea level rises again, in the model configuration including permafrost, there is a strong pulse of downward flow following partial melting of the permafrost (Fig. 10h).

It is possible that this flow, which lasts a few thousand years, is an artifact of the elastic model configuration, in which the release of a load (by submergence of the upper sediment column into the ocean) provokes the expansion of pore spaces in the sediment. However, the model configuration without the sealing effect of permafrost does not show this pulse of invasive flow on sea level rise.

3.3.4 Methane fluxes

There are multiple ways in which the glacial cycles of sea level and air and water temperature might impact the flux of methane to the atmosphere. Submergence in the ocean is one modulating factor, because the emerging bubbles dissolve in the ocean rather than reaching the atmosphere. Another factor is the deposition of high-POC surface soils during low sea level stands, and its exposure to degradation later when the permafrost soils melt. A third factor is permafrost, impeding gas and fluid flow and excluding dissolved methane from ice formation. The impacts of these processes are assessed by comparing the results from model configurations with and without each process in question.

The evolution of the dissolved methane disequilibrium condition ($CH_4/CH_{4\ sat}$) is shown in Fig. 11. At the initiation of the glacial cycles, methane is undersaturated in near-surface sediments on the continental shelf, by diffusive contact with the methane-free ocean upper boundary condition. In the prefreshened sediment column scenario (Fr), methane concentrations in the depth range of 100–1000 m are lower than in the marine case (Mar, Fig. 11b), due to the ventilation by the hydrological pump (Fig. 11a). Further freshening of the pore waters in the ice-free case (SL + LD) tends to deplete methane in the upper sediment column (Fig. 11c–e), while methane exclusion from the permafrost ice leads to supersaturation in simulation GL + LD (Fig. 11f–h). The hydrate stability zone is somewhat expanded in the prefreshened sediment column relative to the marine case (Fig. 11g vs. h, heavy black contour).

Figure 12 shows snapshots of various aspects of the shelf carbon cycle. Sections of POC concentration in Fig. 12, left show the accumulation of POC-rich Yedoma deposits

on land (Fig. 12g and j). The rate of methane production in the model (Fig. 12, right) depends on temperature and organic carbon age, but it is also attenuated by permafrost formation in the model, scaling to zero in the completely frozen case. Methanogenesis rates are near zero in the permafrost zone during glacial time (Fig. 12h), but partially recover during interglacial time (Fig. 12k) even though permafrost is still present.

A zone of methane hydrate stability exists below the permafrost zone when permafrost is present, and some methane hydrate accumulates in that zone. The highest pore-fraction values are found near the continental slope, where the shelf stability field outcrops within the slope depocenter. Dissolved methane concentrations exceed saturation within the stability zone in the model (Fig. 11), but the accumulation of methane hydrate (Fig. 12, right) is limited by the slow rate of methane production. A time series of the inventory of methane as hydrate on the shelf is shown in Fig. 13. The integration cuts off at $x = 560$ km to exclude the sediment depocenter on the continental slope. The inventory of methane in hydrates rises to maxima of ~25 Gt C, right at the deglaciation. However, this methane hydrate cycling is not as significant to the larger carbon cycle as one might expect, because the hydrate is only a small fraction of the dissolved methane pool (which exceeds 1000 Gt C in shelf porewaters of the model).

The impact of the glacial cycles on the methane pathway to the atmosphere in the model is shown in Fig. 14. When sea level is high, the efficiency of bubble transport across the sediment-water interface reaching the atmosphere ranges from about 75 % near the coast to about 10 % at the shelf break (Fig. 14a). Most of the methane flux from the sediment is located just off the shelf break (Fig. 14e), where the escape efficiency is low, so not much methane makes it to the atmosphere during the interglacial. During glacial times, the sediment column is exposed to the atmosphere, and the escape efficiency in the model is 100 % (Fig. 14b). Permafrost inhibits the terrestrial methane flux (Fig. 14i) relative to the case without permafrost (Fig. 14f). During some of the deglaciations, the release of pent-up gas by permafrost degradation leads to a deglaciation spike of excess methane flux to the atmosphere (Fig. 14j–k relative to g–h).

Time series plots of the methane cycle on the continental margin are shown in Fig. 15. The methanogenesis rates in the model output are in units of moles per meter of coastline, since it is a 2-D model. We scale this up to the Siberian continental margin by assuming a width of 1000 km. The area of the shelf is then $5 \times 10^{11} m^2$, roughly comparable to the real shelf area of 460 000 km^2 (Stein and Fahl, 2000).

The biological rate of methane production on the continental shelf evolves through time in Fig. 15b. Yedoma deposition (case SL + LD) tends to slowly increase the total shelf respiration rate in the model, relative to a case with no land deposition (case SL). The formation of permafrost, during glacial periods of case GL + LD, attenuates methaneogenesis by inhibiting biological activity in the frozen soil.

The continental shelf methane cycle is summarized for four different model scenarios in Fig. 15c–f. Results are shown with and without permafrost formation, and with and without the hydrological pre-freshening in the initial condition. Solid regions are cumulative methane sinks. The red lines are the methane source from biological processes. In steady state, where sinks balance sources, the colored areas should fill up the region below the red line.

By model design, permafrost formation inhibits methane loss from the shelf sediments as bubbles. This can be seen in the collapse of the blue region in Fig. 15c and e during times of low sea level. There is no direct link between ice fraction and methane oxidation in the model, which is driven only by coexisting concentrations of sulfate and methane, but the rate of methane oxidation also drops to negligible during glacial times in the simulations with permafrost (grey in Fig. 15c and e).

The only remaining sink for methane from the continental shelf sediment column is offshore subsurface ground water flow carrying dissolved methane (brown in Fig. 15c and e). Offshore transport is also significant or dominant in the runs without permafrost formation (Fig. 15d and f). During interglacial intervals, there is a small onshore flow of dissolved methane into the continental shelf region, for example at time 0, which is indicated in the plot as a negative starting point for the grey region, representing methane oxidation in the sediment column.

Trapping of methane by impermeable permafrost leads to a spike of methane fluxes at the ends of deglaciations in simulations with permafrost (Fig. 15c and e). The spikes happen as sea level approaches its highest extent, stifling the offshore groundwater flow by decreasing the pressure head, but early in the interglacial time while permafrost is the most intact. The spikes are stronger for the first glacial cycles than the last, apparently due to long-term adjustment of the methane cycle on the shelf (a growing together of the production rate (red lines in Fig. 15c–f) and the various methane sinks (colored areas).

The impacts of salinity, prefreshened vs. marine initial conditions, on the methane flux to the atmosphere, are shown in Fig. 16. Due to the differing deposition history, the continental shelf is narrower in the marine than it is for the pre-freshened initial condition simulations. The generally lower fluxes in the shelf methane cycle for the marine case are to some extent due to the differing areas of integration (spanning 460 vs. 560 km of shelf width). The impacts of the pore water salt inventory are most apparent during the time of sea level fall, with permafrost formation (red lines). The saltier sediment column takes about 20 kyr to choke off the methane flux to the atmosphere (Fig. 16a), while the pre-freshened sediment column stops the methane flux more abruptly, in just a few thousand years (Fig. 16b).

In general, the dominant player of the glacial/interglacial cycles on the atmospheric release rate of methane in the model is dissolution of methane bubbles rising through the water column.

3.4 Anthropogenic global warming

The global warming (GW) scenario begins from a high sea-level interglacial state, and raising the temperature following the climate impact of the "spike and long tail" time distribution of a slug of new CO_2 added to the atmosphere (Archer et al., 2009) (Fig. 8). There is a stage of fast atmospheric drawdown as CO_2 invades the ocean, but once the ocean, atmosphere, and land surface reach equilibrium (after a few hundred years), the CO_2 content of the entire biosphere begins to slowly relax toward an initial "natural"

value, by weathering reactions with carbonate and siliceous solid rocks. The net result is a CO_2 drawdown that can be expressed as the sum of several exponential functions in time, with time scales ranging from 10^2–10^6 years. Changes in water column temperature are assumed equal to those of the atmosphere, following paleoceanographic reconstructions (Martin et al., 2002) and long-term coupled ocean/atmosphere circulation model experiments (Stouffer and Manabe, 2003). The first global warming scenario imposes this temperature change on the water column, relaxing toward equilibrium with the atmospheric CO_2 trajectory with a time constant of 100 years.

The effect of sea level rise is added to create a second global warming scenario GW+SL. On time scales of thousands of years the sea level response to changing global temperature is much stronger than the sea level response over the coming century, as prominently forecast by the IPCC. Reconstruction of sea level and global temperature covariation in the geologic past (glacial time to Eocene hothouse) reveals a covariation of 10–20 m $^{\circ}C^{-1}$ (Archer and Brovkin, 2008). The global warming with sea level scenario assumes an equilibrium sea level response of 15 m $^{\circ}C^{-1}$, which it relaxes toward with a time constant of 1000 years.

The atmospheric methane fluxes, shown in Fig. 17, increase in the global warming (GW) model run, as they also do in the control (Ctl) simulation, which is essentially an extended but unwarmed interglacial period. The permafrost melts on a time scale of about 10 000 years for the GW simulation, and about 50 000 for the Ctl. The rates of methane production, and flux to the atmosphere, both increase with the loss of the permafrost, if there is no change in sea level. However, the new methane flux comes not as a sudden burst, but rather as a slow transition toward a new, higher, chronic release rate. When sea level is also changed (GW+SL), bubbles dissolve in the water column, which more than counteracts the increase in methane flux due to the extended interglacial (Ctl) or warming (GW) scenarios.

4 Implications of the model results for the real Siberian continental margin

This is the first simulation of the full methane cycle on the Siberian continental margin, or any other location with embedded permafrost soils, including hydrate formation and transient fluxes. It is internally consistent, linking processes from the ocean, the sea floor, and the deep Earth, within constraints of sediment accommodation and conservation of carbon, through geologic time. As such it has some lessons to teach us about the real Siberian continental margin. However, many of the model variables are not well constrained, such as the methaneogenesis rates or soil permeabilities, meaning that in some aspects the model results are not a strong constraint on reality.

The absolute values of the methane inventories in the system, as hydrate and bubbles, are not well constrained theoretically. The rate of methane production in shallow sediments is not well characterized. In reality there might be some flux of methane from the crust, but this is not included in the simulation. The transport of bubbles through the sediment column is mechanistically poorly understood, therefore not well represented in the code, which affects the inventories of bubbles in the sediment. Ultimately the bubble concentration in the model reaches a rough steady state where production of methane gas balances its escape through the sediment column, but the steady state concentration from the model could be wrong. The model lacks faults, permeable layers, or the ability to "blow out", producing the sedimentary wipe-out zones observed seismically in the subsurface (Riedel et al., 2002), and the pockmarks at the sediment surface (Hill et al., 2004). On land, the model lacks seasonal melting of surface permafrost (to form the active layer) and the thaw bulbs underneath lakes and rivers. In the ocean, the intensity of water column dissolution of rising bubbles depends on the bubble sizes, which depend on the gas emission rate, ultimately driven by details of gas transport in the sediment, which are neglected in the model.

These uncertainties all affect the flux of methane to the atmosphere, which is therefore not well constrained by the model. However, the model is consistent with observations (Kort et al., 2012), that the total atmospheric methane flux from the Siberian

margin is a small fraction of the global flux of methane to the atmosphere, and thus represents only a minor climate forcing. The model would have to be pushed very hard (as would the measurements) to fundamentally change this conclusion.

The model bubble flux to the atmosphere in analog present-day conditions is only 0.02 Tg CH_4 yr^{-1}, which is an order of magnitude lower than an estimate of the total methane emission rate from aircraft (Kort et al., 2012) of 0.3 Tg CH_4 yr^{-1}. The model does not include gas exchange evasion of methane from the water column. Concentrations of methane in the water column of 50 nM are common (Shakhova et al., 2010a), which, if they were unimpeded by sea ice, could lead to a flux from the region of 0.4 Tg CH_4 yr^{-1} (assuming a typical gas exchange piston velocity of 3 m day^{-1}). Methane dissolves into the water column in the model at rates up to 0.4 Tg CH_4 yr^{-1} during times of relatively high sea level. Once released to the water column, the fate of a methane molecule will depend on its lifetime with respect to oxidation, which could be up to a year in the open water column (Valentine et al., 2001), vs. its lifetime with respect to gas exchange, which for ice-unimpeded conditions would be just a few months for a 50 m deep water column. Thus the methane in bubbles dissolving in the water column has some chance of making it to the atmosphere anyway, depending on stratification in the water column and the extent of ice, and the gas exchange flux has the potential to be significant in the regional total flux.

One probably robust feature of the model is the dominant impact of sea level inundation of the sediment column on the atmospheric methane flux. The methane flux is highest during cold times, because sea level is low, rather than providing a positive climate feedback of releasing methane during warm (high sea level) intervals. There is a warming positive feedback in the simulated future from climate warming, but it is much smaller than the impact of sea level changes in the past. The potential for future sea level change is much higher for the deep future, thousands of years from now, than the forecast for the year 2100, because it takes longer than a century for ice sheets to respond to changes in climate. The model finds that for the future, if sea level changes by tens of meters, as guided by paleoclimate reconstructions (Archer and Brovkin,

2008), the impact of sea level rise could overwhelm the impact of warming. The dominance of sea level over temperature in the model of this area is due to dissolution of methane in the water column, rather than a pressure effect on hydrate stability, which is generally a weaker driver than ocean temperature in deeper-water settings (Mienert et al., 2005).

Another seemingly robust model result is the exclusion of methane hydrate from the permafrost zone, by competition for water between ice and hydrate. This behavior implies that any hydrate on the continental shelf must be at least 300 m below the sea floor in the sediment column (as opposed to as shallow as 100 m when the water activity is held constant, Romanovskii et al., 2005). The insulating layer of sediment should act to slow the time scale for the response to ocean warming, to thousands of years (Archer, 2007). Shakhova et al. (2010b) proposed that 50 Gt C as methane could erupt from the Arctic on a time scale of a few years. As has been acknowledged, the model provides poor constraint on the standing stock of bubbles or methane hydrate in the sediment column, and neglects many of the mechanisms that could come into play in transporting methane quickly to the atmosphere, such faults, channels, and blowouts of the sediment column. However, it is clear that the time scale for ocean warming to perturb methane hydrates that are at least 300 m below the sea floor will be much slower than a few years, leading to the expectation, consistent with the global warming simulations of the model, that the methane cycle on the shelf should take thousands of years to respond to a climate change. The magnitude, and the time scale, of the model response ensures that nothing the model can do would generate such a large abrupt methane eruption. An abrupt release would therefore require a large, contiguous gas pocket suddenly released by melting permafrost, like Arctic lakes that drain away overnight. But 50 Gton of C represents a large fraction of all the traditional natural gas deposits on Earth (about 100 Gt C). The place to look for such a large unstable gas reservoir is in the field, not in this model, but until such a thing is found it remains conjecture.

The Supplement related to this article is available online at doi:10.5194/bgd-11-7853-2014-supplement.

References

Archer, D.: Methane hydrate stability and anthropogenic climate change, Biogeosciences, 4, 521–544, doi:10.5194/bg-4-521-2007, 2007.

Archer, D. and Brovkin, V.: The millennial lifetime of fossil fuel CO_2, Climatic Change, 90, 283–297, 2008.

Archer, D. E., Eby, M., Brovkin, V., Ridgewell, A. J., Cao, L., Mikolajewicz, U., Caldeira, K., Matsueda, H., Munhoven, G., Montenegro, A., and Tokos, K.: Atmospheric lifetime of fossil fuel carbon dioxide, Annu. Rev. Earth Pl. Sc., 37, 117–34, 2009.

Archer, D. E., Buffett, B. A., and McGuire, P. C.: A two-dimensional model of the passive coastal margin deep sedimentary carbon and methane cycles, Biogeosciences, 9, 2859–2878, doi:10.5194/bg-9-2859-2012, 2012.

Cramer, B. and Franke, D.: Indications for an active petroleum system in the Laptev Sea, NE Siberia, J. Petrol. Geol., 28, 369–383, 2005.

Dallimore, S. R. and Collett, T. S.: Intrapermafrost gas hydrates from a deep core-hole in the Mackenzie delta, Northwest-Territories, Canada, Geology, 23, 527–530, 1995.

Dutta, K., Schuur, E. A. G., Neff, J. C., and Zimov, S. A.: Potential carbon release from permafrost soils of Northeastern Siberia, Glob. Change Biol., 12, 2336–2351, 2006.

Gavrilov, A. V., Romanovskii, X. N., Romanovsky, V. E., Hubberten, H. W., and Tumskoy, V. E.: Reconstruction of ice complex remnants on the eastern Siberian arctic shelf, Permafrost Periglac., 14, 187–198, 2003.

Gentz, T., Damm, E., von Deimling, J. S., Mau, S., McGinnis, D. F., and Schluter, M.: A water column study of methane around gas flares located at the West Spitsbergen continental margin, Cont. Shelf Res., 72, 107–118, 2014.

Gilichinsky, D., Rivkina, E., Bakermans, C., Shcherbakova, V., Petrovskaya, L., Ozerskaya, S., Ivanushkina, N., Kochkina, G., Laurinavichuis, K., Pecheritsina, S., Fattakhova, R., and Tiedje, J. M.: Biodiversity of cryopegs in permafrost, FEMS Microbiol. Ecol., 53, 117–128, 2005.

Hill, J. C., Driscoll, N. W., Weissel, J. K., and Goff, J. A.: Large-scale elongated gas blowouts along the US Atlantic margin, J. Geophys. Res.-Sol. Ea., 109, B09101, doi:10.1029/2004JB002969, 2004.

Hunt, J. M.: Petroleum Geochemistry and Geology, Freeman, New York, 743 pp., 1995.

Khvorostyanov, D. V., Ciais, P., Krinner, G., Zimov, S. A., Corradi, C., and Guggenberger, G.: Vulnerability of permafrost carbon to global warming. Part II: sensitivity of permafrost carbon stock to global warming, Tellus B, 60, 265–275, 2008a.

Khvorostyanov, D. V., Krinner, G., Ciais, P., Heimann, M., and Zimov, S. A.: Vulnerability of permafrost carbon to global warming. Part I: model description and role of heat generated by organic matter decomposition, Tellus B, 60, 250–264, 2008b.

Kort, E. A., Wofsy, S. C., Daube, B. C., Diao, M., Elkins, J. W., Gao, R. S., Hintsa, E. J., Hurst, D. F., Jimenez, R., Moore, F. L., Spackman, J. R., and Zondlo, M. A.: Atmospheric observations of Arctic Ocean methane emissions up to 82 degrees north, Nat. Geosci., 5, 318–321, 2012.

Martin, P. A., Lea, D. W., Rosenthal, Y., Shackleton, N. J., Sarnthein, M., and Papenfuss, T.: Quaternary deep sea temperature histories derived from benthic foraminiferal Mg/Ca, Earth Planet. Sci. Lett., 198, 193–209, 2002.

Middelburg, J. J., Soetaert, K., and Herman, P. M. J.: Empirical relations for use in global diagenetic models, Deep-Sea Res. Pt. I, 44, 327–344, 1997.

Mienert, J., Vanneste, M., Bunz, S., Andreassen, K., Haflidason, H., and Sejrup, H. P.: Ocean warming and gas hydrate stability on the mid-Norwegian margin at the Storegga Slide, Mar. Petrol. Geol., 22, 233–244, 2005.

Moore, W. S., Carlson, C. A., and Giovannoni, S. J.: The effect of submarine groundwater discharge on the ocean, Ann. Rev. Mar. Sci., 2, 59–88, 2011.

Nicolsky, D. and Shakhova, N.: Modeling sub-sea permafrost in the East Siberian arctic shelf: the Dmitry Laptev strait, Environ. Res. Lett., 5, 015006, doi:10.1088/1748-9326/5/1/015006, 2010.

Nicolsky, D. J., Romanovsky, V. E., Romanovskii, N. N., Kholodov, A. L., Shakhova, N. E., and Semiletov, I. P.: Modeling sub-sea permafrost in the East Siberian arctic shelf: the Laptev Sea region, J. Geophys. Res.-Earth, 117, F03028, doi:10.1029/2012JF002358, 2012.

Portnov, A., Smith, A. J., Mienert, J., Cherkashov, G., Rekant, P., Semenov, P., Serov, P., and Vanshtein, B.: Offshore permafrost decay and massive seabed methane escape in water depths >20 m at the South Kara Sea shelf, Geophys. Res. Lett., 40, 3962–3967, 2013.

Post, V. E. A., Groen, J., Kooi, H., Person, M., Ge, S. M., and Edmunds, W. M.: Offshore fresh groundwater reserves as a global phenomenon, Nature, 504, 71–78, 2013.
Reagan, M. T.: Dynamic response of oceanic hydrate deposits to ocean temperature change, J. Geophys. Res.-Oceans, 113, C12023, doi:10.1029/2008JC004938, 2008.
Reagan, M. T. and Moridis, G. J.: Large-scale simulation of methane hydrate dissociation along the West Spitsbergen Margin, Geophys. Res. Lett., 36, L23612, doi:10.1029/2009GL041332, 2009.
Reagan, M. T., Moridis, G. J., Elliott, S. M., and Maltrud, M.: Contribution of oceanic gas hydrate dissociation to the formation of Arctic Ocean methane plumes, J. Geophys. Res.-Oceans, 116, C09014, doi:10.1029/2011JC007189, 2011.
Riedel, M., Spence, G. D., Chapman, N. R., and Hyndman, R. D.: Seismic investigations of a vent field associated with gas hydrates, offshore Vancouver Island, J. Geophys. Res.-Sol. Ea., 107, 2200, doi:10.1029/2001JB000269, 2002.
Romanovskii, N. N. and Hubberten, H. W.: Results of permafrost modelling of the lowlands and shelf of the Laptev Sea region, Russia, Permafrost Periglac., 12, 191–202, 2001.
Romanovskii, N. N., Hubberten, H. W., Gavrilov, A. V., Tumskoy, V. E., Tipenko, G. S., Grigoriev, M. N., and Siegert, C.: Thermokarst and land-ocean interactions, Laptev Sea Region, Russia, Permafrost Periglac., 11, 137–152, 2000.
Romanovskii, N. N., Hubberten, H. W., Gavrilov, A., Tumskoy, V. E., and Kholodov, A. L.: Permafrost of the east Siberian Arctic shelf and coastal lowlands, Quaternary Sci. Rev., 23, 1359–1369, 2004.
Romanovskii, N. N., Hubberten, H. W., Gavrilov, A. V., Eliseeva, A. A., and Tipenko, G. S.: Offshore permafrost and gas hydrate stability zone on the shelf of East Siberian seas, Geo-Mar. Lett., 25, 167–182, 2005.
Schuur, E. A. G., Bockheim, J., Canadell, J. G., Euskirchen, E., Field, C. B., Goryachkin, S. V., Hagemann, S., Kuhry, P., Lafleur, P. M., Lee, H., Mazhitova, G., Nelson, F. E., Rinke, A., Romanovsky, V. E., Shiklomanov, N., Tarnocai, C., Venevsky, S., Vogel, J. G., and Zimov, S. A.: Vulnerability of permafrost carbon to climate change: implications for the global carbon cycle, Bioscience, 58, 701–714, 2008.
Shakhova, N.: Geochemical and geophysical evidence of methane release over the East Siberian arctic shelf, J. Geophys. Res.-Oceans, 115, 190–193, doi:10.1029/2009JC005602, 2010.

Shakhova, N., Semiletov, I., and Panteleev, G.: The distribution of methane on the Siberian Arctic shelves: implications for the marine methane cycle, Geophys. Res. Lett., 32, L09601, doi:10.1029/2005GL022751, 2005.
Shakhova, N. E., Nicolsky, D. Y., and Semiletov, I. P.: Current state of subsea permafrost on the East Siberian shelf: tests of modeling results based on field observations, Dokl. Earth Sci., 429, 1518–1521, 2009.
Shakhova, N., Semiletov, I., Salyuk, A., Yusupov, V., Kosmach, D., and Gustafsson, O.: Extensive methane venting to the atmosphere from sediments of the East Siberian arctic shelf, Science, 327, 1246–1250, 2010a.
Shakhova, N. E., Alekseev, V. A., and Semiletov, I. P.: Predicted methane emission on the East Siberian shelf, Dokl. Earth Sci., 430, 190–193, 2010b.
Stein, R. and Fahl, K.: Holocene accumulation of organic carbon at the Laptev Sea continental margin (Arctic Ocean): sources, pathways, and sinks, Geo-Mar. Lett., 20, 27–36, 2000.
Stouffer, R. J. and Manabe, S.: Equilibrium response of thermohaline circulation to large changes in atmospheric CO_2 concentration, Clim. Dynam., 20, 759–773, 2003.
Taylor, A. E., Dallimore, S. R., and Outcalt, S. I.: Late quaternary history of the Mackenzie-Beaufort region, Arctic Canada, from modelling of permafrost temperatures. 1. The onshore offshore transition, Can. J. Earth Sci., 33, 52–61, 1996.
Valentine, D. L., Blanton, D. C., Reeburgh, W. S., and Kastner, M.: Water column methane oxidation adjacent to an area of active hydrate dissociation, Eel River Basin, Geochim. Cosmochim. Ac., 65, 2633–2640, 2001.
Verrjuit, A.: A note on the Ghyben–Herzberg formula, Bull. Int. Assoc. Sci. Hydrol., 13, 43–46, 1968.
Walter, K. M., Zimov, S. A., Chanton, J. P., Verbyla, D., and Chapin, F. S.: Methane bubbling from Siberian thaw lakes as a positive feedback to climate warming, Nature, 443, 71–75, 2006.
Westbrook, G. K., Thatcher, K. E., Rohling, E. J., Piotrowski, A. M., Paelike, H., Osborne, A. H., Nisbet, E. G., Minshull, T. A., Lanoiselle, M., James, R. H., Huehnerbach, V., Green, D., Fisher, R. E., Crocker, A. J., Chabert, A., Bolton, C., Beszczynska-Moeller, A., Berndt, C., and Aquilina, A.: Escape of methane gas from the seabed along the West Spitsbergen continental margin, Geophys. Res. Lett., 36, L15608, doi:10.1029/2009GL039191, 2009.

Zimov, S. A., Davydov, S. P., Zimova, G. M., Davydova, A. I., Schuur, E. A. G., Dutta, K., and Chapin III, F. S.: Permafrost carbon: stock and decomposability of a globally significant carbon pool, Geophys. Res. Lett., 33, L20502, doi:10.1029/2006GL027484, 2006.

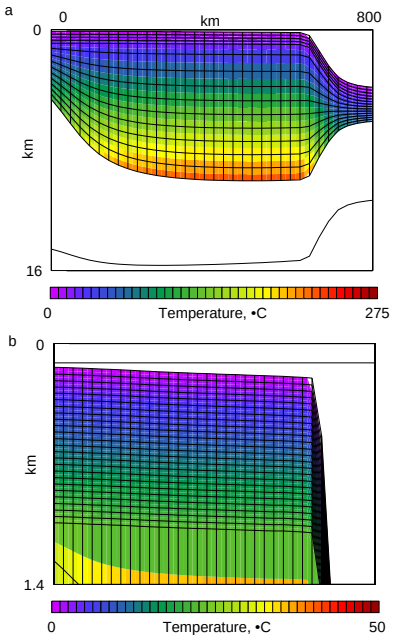

Figure 1. Domain of the model as applied to the Laptev Sea continental shelf and slope. This is the result of 62 million years of sediment accumulation on the crust, isostatic subsidence, pore fluid flow, and thermal diffusion, used as the initial condition for glacial/interglacial cycle and climate change simulations. Color indicates temperature. **(a)** Full view. Black line shows the bottom of the crust, which grades smoothly from continental on the left into ocean crust through most of the domain on the right. **(b)** Zoom in to see increased model resolution in the upper kilometer of the sediment column.

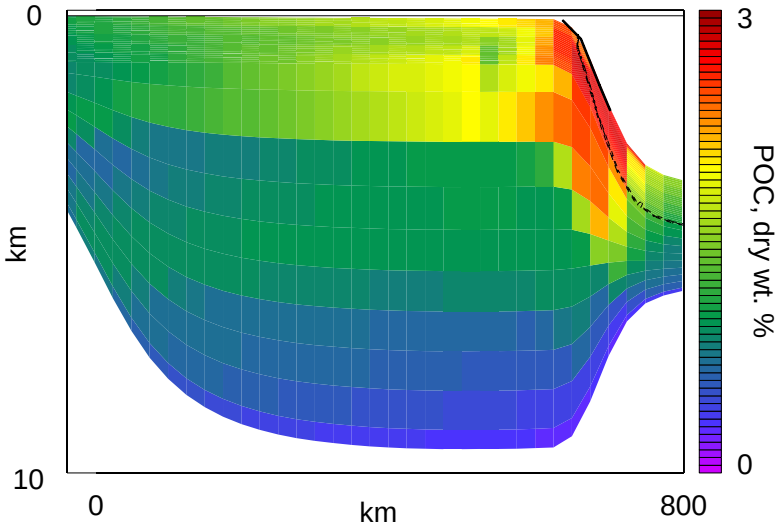

Figure 2. Particulate Organic Carbon (POC) concentration. Highest values are found in the sediment depocenter just off the continental shelf break.

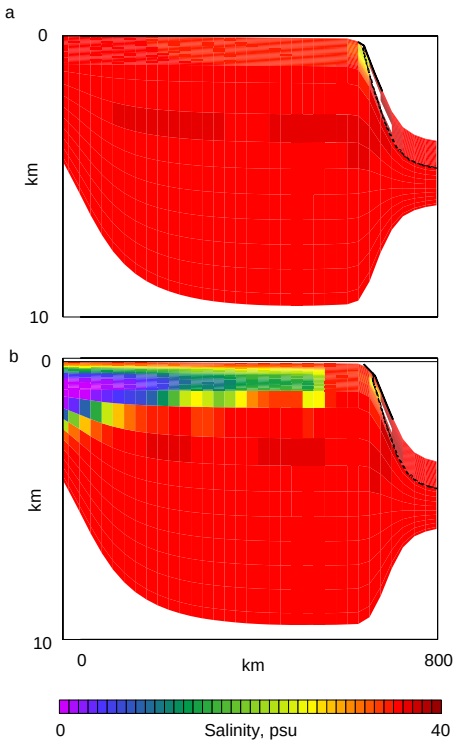

Figure 3. Pore water salinity. **(a)** The fully marine case, in which the sediment column has always been submerged underneath a time-invariant sea level. **(b)** Result of sediment column freshening by hydrological groundwater flow, driven by the pressure head resulting from a water table higher than sea level. A movie of the transition from a to b can be seen at http://geosci.uchicago.edu/~archer/spongebob_arctic/sal.65e6.nc.drop120.movie.gif.

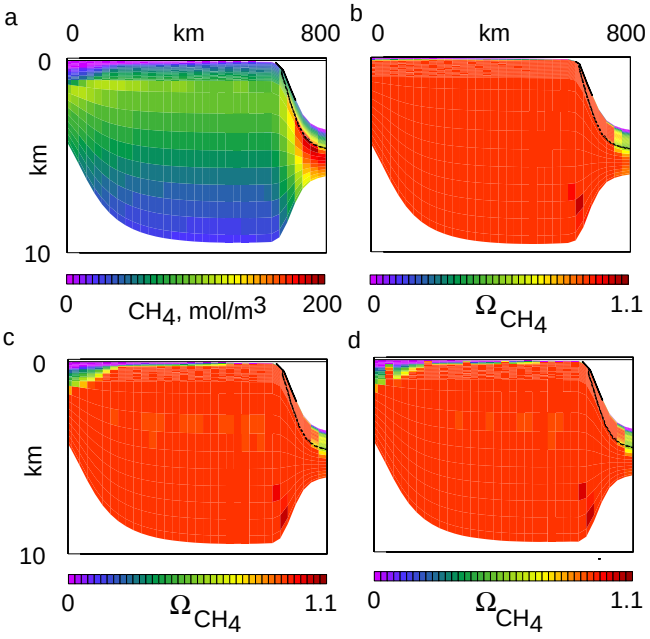

Figure 4. Initial distribution of dissolved methane. **(a)** Concentration in moles m^{-3}. **(b–d)** $\Omega = CH_4/CH_{4(sat)}$ deviation from equilibrium, **(b)** of the Marine (salty) initial condition; **(c)** of the pre-freshened initial condition (note depletion in near-surface near-shore sediments in the upper left); **(d)** including permeable channels every five grid points, plus pre-freshening.

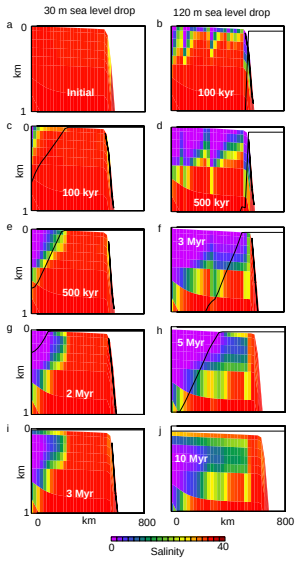

Figure 5. Freshening the sediment column by hydrological groundwater flushing. Color indicates salinity. Solid black line represents sea level in the ocean (white space), and the equilibrium fresh-salty boundary given a snapshot of the pressure head (the Ghyben–Herzberg relation). Left side: results of dropping sea level 30 m and holding it there. A freshwater lens forms and strives to reach Ghyben Herzberg equilibrium as the sediment column subsides, where atmospheric exposure decreases its buoyancy and stops sediment accumulation. After the sediment column subsides beneath the still-lowered sea level, the fresh water lens remains for millions of years. A movie can be seen at http://geosci.uchicago.edu/~archer/spongebob_arctic/sal.zoom.65e6.nc.drop030.movie.gif. Right side: Result of dropping sea level 120 m and holding it there forever. Movie at http://geosci.uchicago.edu/~archer/spongebob_arctic/sal.zoom.65e6.nc.drop120.movie.gif.

Discussion Paper | Discussion Paper | Discussion Paper | Discussion Paper |

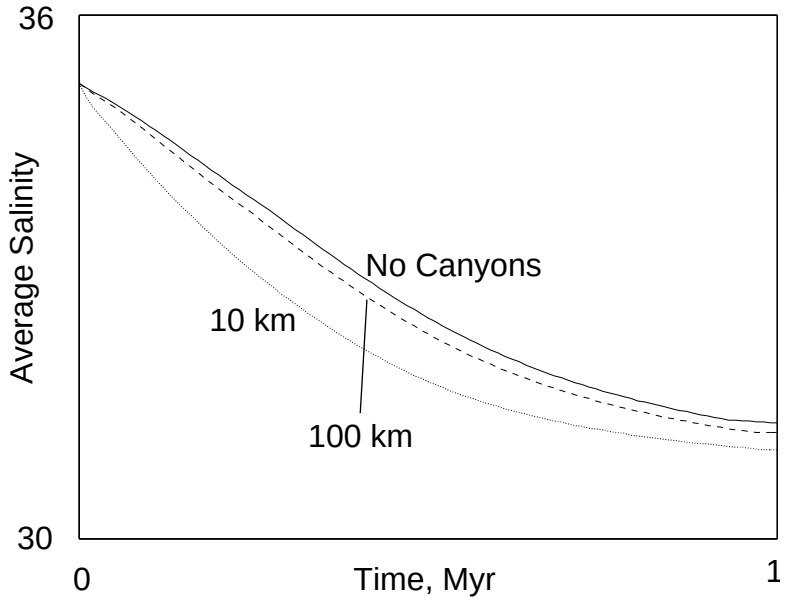

Figure 6. Time scale of depleting the salinity of the continental shelf sediment column after an instantaneous sea level drop of 30 m. The effect of lateral canyons is to provide a pathway for saline fluid to be replaced by fresh groundwater in sediments above sea level. If the lateral canyon spacing is 10 km, they can have a significant impact on the time constant for ground water flushing. A more conservative 100 km canyon is adopted for the rest of the simulations.

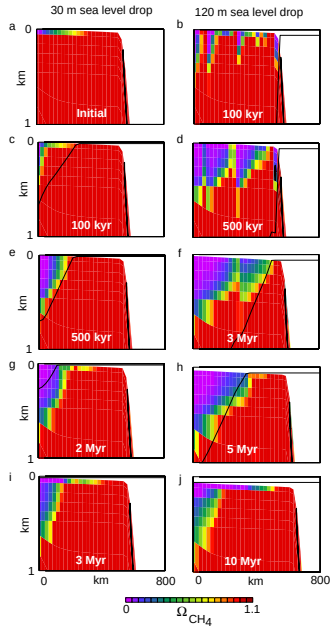

Figure 7. Dissolved methane impact by hydrological freshening of the sediment column as described in Fig. 5. $\Omega = CH_4/C_{4(sat)}$. Movies can be seen at http://geosci.uchicago.edu/~archer/spongebob_arctic/d_ch4.65e6.nc.drop030.movie.gif and http://geosci.uchicago.edu/~archer/spongebob_arctic/d_ch4.65e6.nc.drop120.movie.gif.

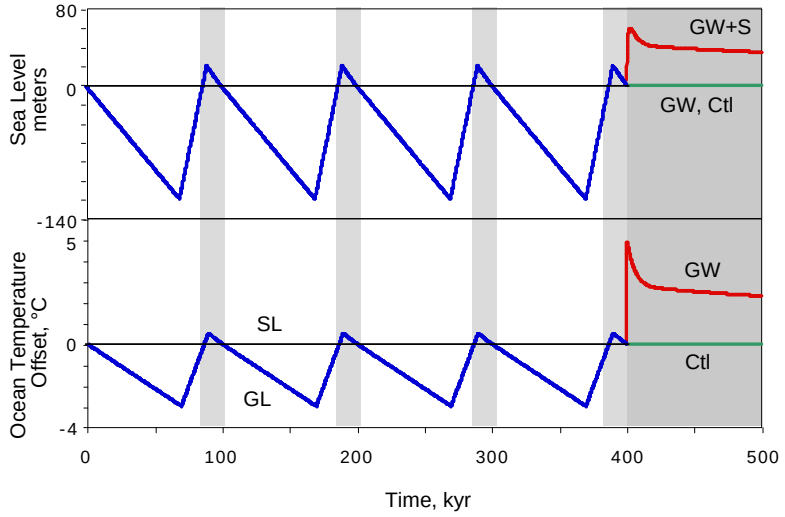

Figure 8. Time-dependent forcing for the glacial/interglacial simulations and the global warming scenarios. **(a)** Sea level is imposed as a sawtooth 100 kyr cycle, with interglacial intervals shaded. The GW + S simulation tracks potential changes in sea level on long time scales due to fossil fuel CO_2 release, following a covariation from the geologic past of 15 m °C^{-1}. The GW and Control simulations hold sea level at interglacial levels. **(b)** Ocean temperature forcings.

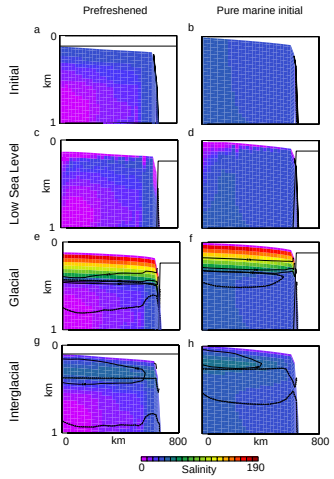

Figure 9. Colors indicate salinity in the unfrozen pore fluid of the sediment column. Thin solid black contours show the frozen fraction of the pore space. Heavy black stippled contour shows the stability boundary of methane hydrate as a function of temperature, pressure, and unfrozen pore fluid salinity. Left side: previously pre-freshened initial condition. Right side: pure marine initial condition. (**c** and **d**) Lowered sea level (from 70 kyr in Fig. 8) but warm air temperatures prevent permafrost formation. (**e** and **f**) Glacial conditions of lowered sea level (70 kyr) and atmospheric temperature of −17 °C driving permafrost formation. The pre-freshened and the marine initial conditions differ in the frozen fraction of sediment, but the salinity of the unfrozen fluid, a correlate of the activity of water, depends only the temperature. (**g** and **h**) Rising sea level (at 90 kyr in Fig. 8) into an interglacial interval. A movie of the pre-freshened simulation can be seen at http://geosci.uchicago.edu/~archer/spongebob_arctic/sal.zoom.65e6.nc.ld2.gl.pfb.movie.gif, and the marine simulation at http://geosci.uchicago.edu/~archer/spongebob_arctic/sal.zoom.65e6.nd.nc.ld2.gl.pfb.movie.gif.

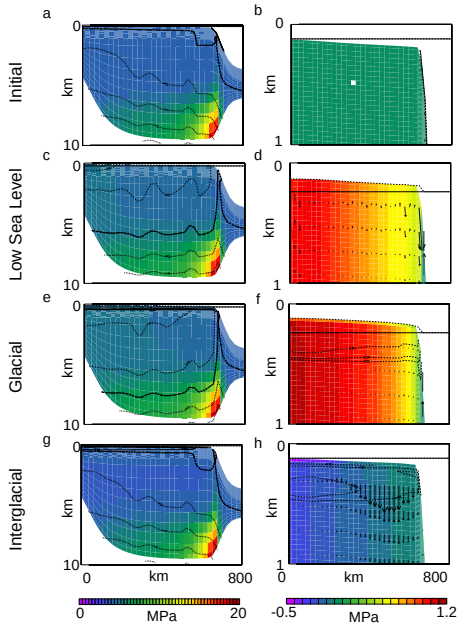

Figure 10. Pore fluid pressure forcing and flow through the glacial cycles. (Left) Colors indicate $P_{excess} + P_{head}$, solid contours are ice fraction, dashed contours are P_{head}. (Right) Colors indicate $P_{excess} + P_{head}$, note different color scale from Left. Dashed contours indicate ice fraction, vectors fluid velocity. Movies can be seen at http://geosci.uchicago.edu/~archer/spongebob_arctic/press_uw.65e6.nc.ld2.gl.pf_eq.gw.comp.movie.gif and http://geosci.uchicago.edu/~archer/spongebob_arctic/pressure_flow.65e6.nc.ld2.gl.pf_eq.gw.comp.movie.gif.

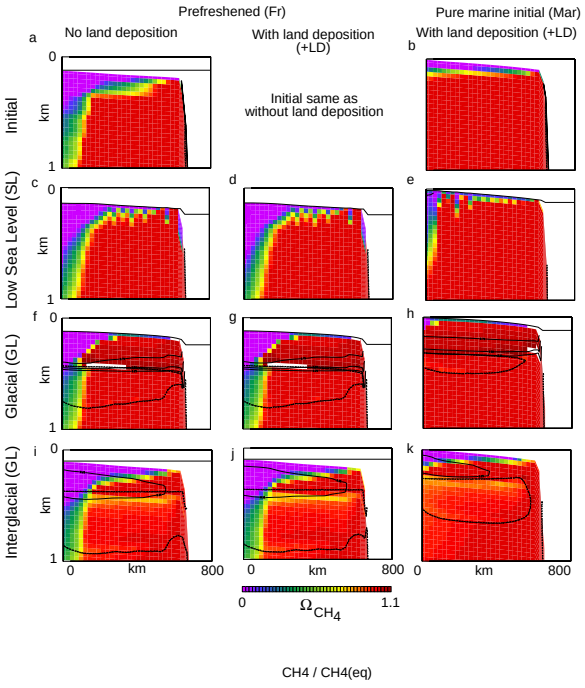

Figure 11. Dissolved methane concentration relative to equilibrium ($\Omega = CH_4/CH_{4(sat)}$). Solid contours indicate ice fraction, dashed contours show the methane hydrate stability boundary. Movies at http://geosci.uchicago.edu/~archer/spongebob_arctic/d_ch4.65e6.nc.gl.pfb.movie.gif, http://geosci.uchicago.edu/~archer/spongebob_arctic/d_ch4.65e6.nc.ld2.gl.pfb.movie.gif, and http://geosci.uchicago.edu/~archer/spongebob_arctic/d_ch4.65e6.nd.nc.ld2.gl.pfb.movie.gif for the left, center, and right columns, respectively.

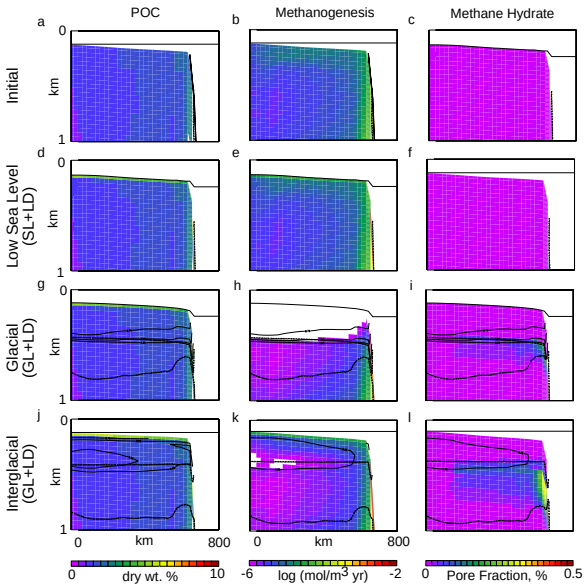

Figure 12. Solid contours: ice Fraction. Dashed contours: methane hydrate stability zone. (Left) Particulate organic carbon (POC) concentration. Movie at http://geosci.uchicago.edu/~archer/spongebob_arctic/poc.65e6.nc.ld2.gl.pfb.movie.gif. (Center) Biological methane production rate. Movie at http://geosci.uchicago.edu/~archer/spongebob_arctic/ch4_src.65e6.nc.ld2.gl.pfb.movie.gif. (Right) Methane hydrate concentration. Movie at http://geosci.uchicago.edu/~archer/spongebob_arctic/hydrate_bubbles_zoom.65e6.nc.ld2.gl.pfb.movie.gif.

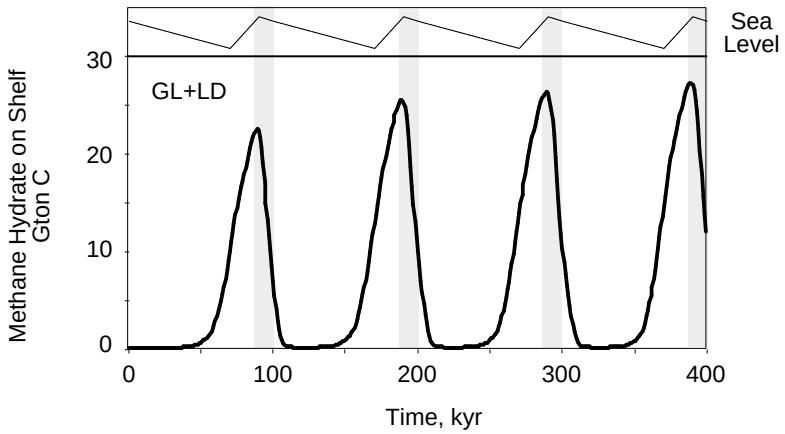

Figure 13. Glacial cycle of methane hydrate inventory on the continental shelf for the simulation including permafrost formation.

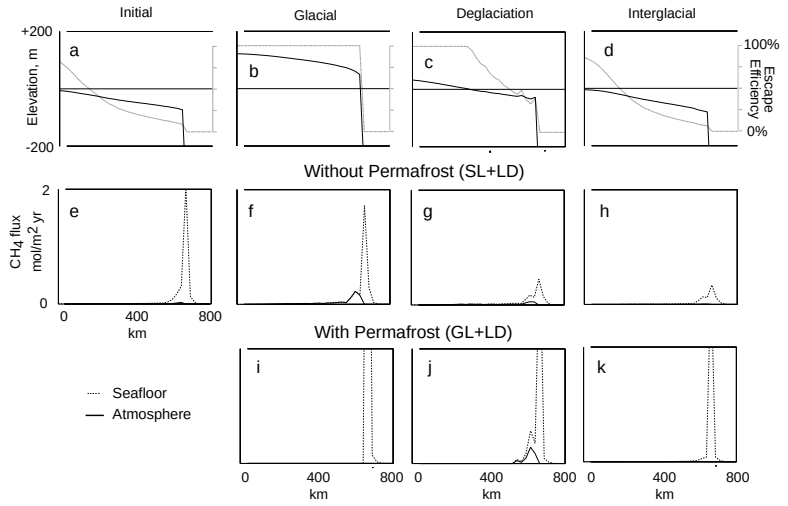

Figure 14. Spatial distribution and sea level impact of methane fluxes to the atmosphere. **(a–d)** Solid line shows the elevation of the sediment surface relative to the sea level at the time. Grey lines (scale to right) show the efficiency of bubble transport through the water column, assuming a flux attenuation length scale of 30 m. **(e–k)** Dashed line: methane bubble flux across the sediment surface. Solid line: methane bubble flux to the atmosphere (dashed line multiplied by transport efficiency). Most of the methane flux in the model occurs near the shelf break, and submergence in the ocean has a strong impact on the flux to the atmosphere. A related movie can be seen at http://geosci.uchicago.edu/~archer/spongebob_arctic/bubb_atm.65e6.nc.ld2.gl.pfb.gw.comp.movie.gif.

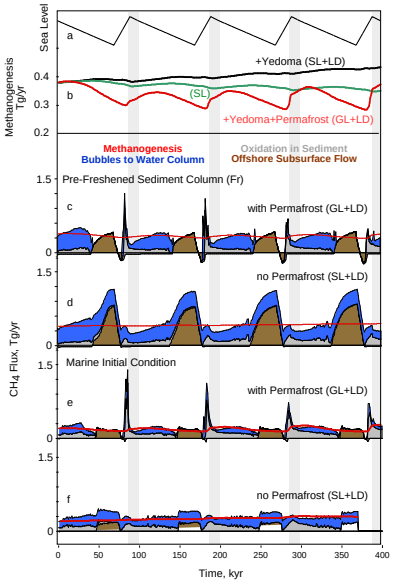

Figure 15. Glacial/interglacial cycle of methane fluxes on the continental margin of the model. **(a)** Sea level driver for reference, grey regions indicate interglacial intervals. **(b)** Biological methane production on the shelf. Green is case SL (sea level changes only), black is SL + LD (adding land deposition of carbon-rich soils), red is GL (adding permafrost formation). **(c–f)** Cumulative methane fluxes. Red lines show production rate. Brown regions show lateral transport of dissolved methane. Grey shows oxidation by SO_4^{2-} in the sediment column. Blue shows bubble flux to the water column. During interglacial times (e.g. far left) there is a small onshore transport of methane, which is represented by a negative starting point for the oxidation (grey) region. In equilibrium, the colored areas should fill in the region under the red curve.

Discussion Paper | Discussion Paper | Discussion Paper | Discussion Paper |

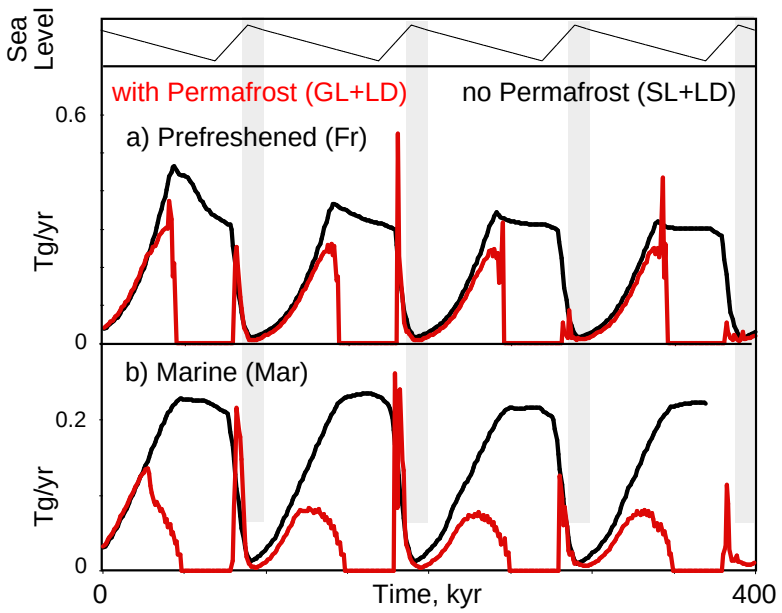

Figure 16. Impact of sediment column pre-freshening and sea level changes on model methane fluxes to the atmosphere. Black lines show results without permafrost formation, red lines are with permafrost. **(a)** From a pre-freshened initial condition, lowering the mean salinity of the sediment column. **(b)** From a pure marine initial condition.

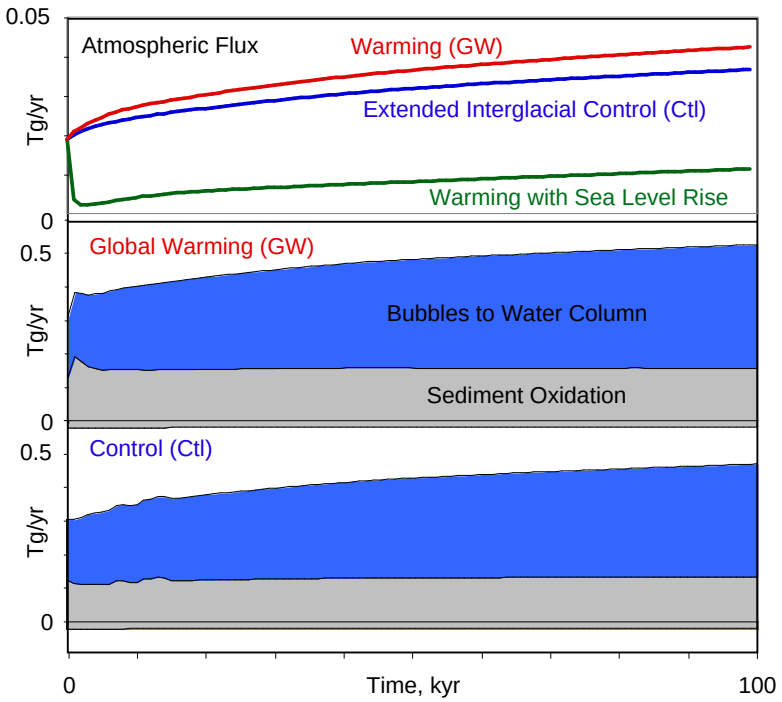

Figure 17. Impact of anthropogenic warming on the methane cycle in the model. The effect of the warming by itself is a slight increase in the methane flux to the atmosphere. Warming + increasing sea level attenuates the methane flux, due to bubble dissolution in a deeper water column.